

RGBlimp-Q: Robotic Gliding Blimp With Moving Mass Control Based on a Bird-Inspired Continuum Arm

Hao Cheng and Feitian Zhang*

Abstract—Robotic blimps, as lighter-than-air aerial systems, offer prolonged duration and enhanced safety in human-robot interactions due to their buoyant lift. However, robust flight against environmental airflow disturbances remains a significant challenge, limiting the broader application of these robots. Drawing inspiration from the flight mechanics of birds and their ability to perch against natural wind, this article introduces RGBlimp-Q, a robotic gliding blimp equipped with a bird-inspired continuum arm. This arm allows for flexible attitude adjustments through moving mass control to enhance disturbance resilience, while also enabling object capture by using claws to counteract environmental disturbances, similar to a bird. This article presents the design, modeling, and prototyping of RGBlimp-Q, thus extending the advantages of robotic blimps to more complex environments. To the best of the authors' knowledge, this is the first interdisciplinary design integrating continuum mechanisms onto robotic blimps. Experimental results from both indoor and outdoor settings validate the improved flight robustness against environmental disturbances offered by this novel design.

Index Terms—Aerial Systems: Mechanics and Control, Flying Robots, Mechanism Design.

I. INTRODUCTION

WITH the rise of aerial vehicle applications comes the need for portable miniature aerial robots capable of low-speed, safe, and long-endurance flight [1]–[3]. In recent years, there has been increasing attention on developing robotic blimps for their prolonged flight endurance and enhanced safety in human-robot interactions [4]–[10]. As a type of lighter-than-air (LTA) aerial vehicle, robotic blimps hold significant potential for applications requiring extended airborne operation at low speeds. Examples include search and rescue missions [6], [11], environmental monitoring [12], [13], human-robot interaction [14]–[16], and entertainment [17], [18]. Unlike heavier-than-air (HTA) robots, such as drones, robotic blimps utilize buoyancy to counteract gravity, leading to lower energy consumption. However, the buoyant nature of these robots makes them sensitive to airflow disturbances, posing a challenge for robust flight, especially in complex outdoor environments. Therefore, enhancing the robust flight capabilities of robotic blimps is imperative to fully exploit their potential for long endurance and safety.

The authors are with the Department of Advanced Manufacturing and Robotics, College of Engineering, Peking University, Beijing 100871, China (e-mail: h-cheng@stu.pku.edu.cn; feitian@pku.edu.cn).

The videos, open-sourced hardware, and source code of this work are available at <https://RGBlimp.github.io>.



Fig. 1. A snapshot of the RGBlimp-Q perching on a branch through the use of the novel continuum arm design (the upper figure), emulating the behavior of a bird, as shown in the lower figure [27].

Numerous efforts in the literature focus on achieving robust flight for robotic blimps through the use of disturbance compensation controllers [19]–[22], a method commonly applied to rotary-wing aerial robots [23]–[26]. However, significant performance distinctions between robotic blimps and rotary-wing aerial robots, such as differences in aerodynamics and thrust arrangement, have been underexplored. This oversight has hindered the application of robust flight control techniques to robotic blimps, like those enabling rotary-wing aerial robots to navigate through outdoor windy environments. To address this challenge, it is imperative to design a novel mechanism for robotic blimps that facilitates robust flight.

Flying lizards and flying squirrels use the inertia of their tails to control their gliding attitude, especially during low-speed flight [28], [29]. Birds, on the other hand, exhibit robust flight by adjusting their wing movements to change attitude in response to wind disturbances [30], [31] and by using their claws to perch on branches, thereby resisting excessive wind [32], [33]. In contrast, current robotic blimps lack an adaptive strategy comparable to these natural mechanisms to withstand wind disturbances.

This article introduces RGBlimp-Q, **the first** robotic gliding blimp equipped with a bionic lightweight continuum arm designed for both moving mass control and object capture.

Building upon our previous work on RGBlimp [7], which utilized hybrid aerodynamic-buoyant lift, RGBlimp-Q features a lightweight continuum arm with a bird-like claw. This arm allows for flexible moving mass control in space, enhancing the robot's ability to control its attitude in the air for improved flight robustness, like flying animals. Furthermore, the bird-like claw mounted at the end of the continuum arm enables the robot to catch objects, addressing a crucial yet often overlooked requirement for robotic blimps. A prototype of RGBlimp-Q has been successfully developed, weighing about 7 g, accounting for net buoyancy. Extensive flight experiments, conducted both indoors and outdoors using a classical feedback controller, validate the effectiveness of the proposed design in enhancing flight maneuverability and robustness.

The contribution of this article is threefold. First, this article proposes RGBlimp-Q, a novel robotic blimp featuring a bionic continuum arm for moving mass control and object capture, thereby extending the advantages of robotic blimps to complex environments with wind disturbance. Second, a unique lightweight continuum arm is designed, equipped with a bird-like claw. Utilizing a decoupled cable-driven mechanism, this design ensures compactness and flexibility, making it ideal for integration into RGBlimp-Q. The claw enables object capture, allowing the robot to rest against wind disturbances, mimicking bird behavior. Third, extensive experiments are conducted both indoors and outdoors, the results of which validate the effectiveness of the design in enhancing flight maneuverability and robustness.

The rest of this article is organized as follows. Section II reviews relevant literature. Section III presents the design and modeling of the RGBlimp-Q, incorporating a continuum arm for moving mass control. Section IV details the design of the decoupled cable-driven continuum arm with a bird-inspired gripper for attitude control and resisting wind disturbances. Section V presents the developed RGBlimp-Q prototype and provides system identification results obtained from steady flight experimental data. Section VI describes indoor and outdoor flight experiments, validating the effectiveness of the proposed design. Finally, Section VII concludes this article.

II. RELATED WORK

A. Robust Flight and Robotic Blimps

Aerial robots are significantly influenced by aerodynamic disturbances resulting from self motion or environmental airflow, making adaptation to such disturbances crucial for robust flight, particularly in complex and uncertain environments. With the rise of rotary-wing aerial robots, significant strides have been made in robust flight control of small-sized aerial vehicles. For example, Wang *et al.* proposed a neural network-based disturbance estimator for achieving robust flight control of a quadrotor, demonstrating its effectiveness through physical flight experiments under disturbances caused by a tether and a fan [23]. Saviolo *et al.* presented a learning uncertainty-aware model prediction controller for a multi-rotor system, facilitating robust flight in challenging real-world flight tests with wind and payload disturbances

[24]. O'Connell *et al.* introduced a learning-based adaptive controller, enabling robust flight of a quadrotor in winds [25]. Powers *et al.* introduced a controller designed to compensate the aerodynamic disturbances caused by ground effect, ensuring robust flight in close proximity to the ground [26].

Robotic Blimps, characterized by buoyant envelopes, prioritize longevity and safety in the air over aerodynamic stability. Therefore, compensating for disturbances is imperative for achieving robust flight of robotic blimps, especially in environments with complex disturbances, such as outdoors. Wang *et al.* proposed robust controllers with disturbance compensation for robust flight control of an indoor robotic blimp prototype [19]. Liu *et al.* presented a reinforcement learning approach for a robotic blimp to enhance flight robustness against wind disturbances [21]. Kawano introduced a motion planning approach considering wind disturbance for robust flight of robotic blimps [22]. Tao *et al.* proposed a feedback controller to reduce the undesired long-standing swinging oscillation caused by the mechanism design and aerodynamic properties of traditional robotic blimps [34]. However, (almost) all robust controllers based on the existing mechanism design of robotic blimps face challenges in replicating the achievement of rotary-wing aerial robots in robust outdoor flight performance. The mechanism design tailored specifically for robotic blimps for robust flight has long been neglected.

B. Aerial Robotic Manipulators and Continuum Arms

The field of aerial robotic manipulators has experienced sustained growth in recent years, with various prototypes demonstrating successful manipulation tasks [1], [2]. One important application is robots perching on support structures, such as branches, using their manipulators to conserve energy or counteract environmental disturbance. Several mechanisms for perching of rotary-wing aerial robots have been proposed, including bio-inspired passive mechanisms and actively-controlled grippers [32], [35]–[37]. For example, Hang *et al.* proposed modularized landing gears for the perching and resting of quadrotors aerial robots [35], while Roderick *et al.* proposed a biomimetic robotic leg and grasper, enabling rotary-wing aerial robots to perch on complex surfaces and catch objects in the air [32]. Although manipulators for perching purposes are rare in fixed-wings aerial robots due to their high-speed flight, there in fact exist some designs for high-speed grasping. For instance, Stewart *et al.* proposed an avian-inspired claw to achieve a catching behavior similar to the swoop and grasp strategy observed in eagles [38].

While aerial robotic manipulations have achieved many milestones, most have focused on integrating conventional rigid robotic arms. Continuum arms offer a promising alternative, thanks to their compact structure, lightweight design, and flexible motion capabilities. This innovative concept features flexible backbone structures with theoretically infinite degrees of freedom [39], [40], utilizing diverse backbone materials such as elastic material [41]–[45], actuated by pneumatic or cable-driven actuators [42]–[45]. To manage this complexity, the piecewise constant curvature (PCC) kinematics is widely adopted [45]–[48]. Recently, a few aerial continuum

manipulators have been developed. For instance, Peng *et al.* presented and integrated an aerial continuum manipulator onto a quadrotor, conducting aerial grasping operations [49].

However, the integration of aerial manipulation mechanisms onto robotic blimps remains an open problem in the literature, regardless of whether they use rigid or continuum arms. In fact, considering both the positive features of long endurance with low speed and the negative aspect of vulnerability to disturbance for such LTA aerial systems, the introduction of such mechanisms for aerial manipulation or perching against wind is both appropriate and necessary. A significant challenge therein lies in the mismatch between the weight of existing manipulators and the limited payload capacity of robotic blimps.

III. RGLBLIMP-Q WITH MOVING MASS CONTROL

To engineer an aircraft suitable for indoor and outdoor low-speed long-term flight, and to enhance its robustness against environmental wind disturbance, we propose the moving mass control-based robotic gliding blimp, RGLblimp-Q. This section investigates the advantages of the moving mass control approach in terms of flight maneuverability and robustness, followed by the presentation of the design and the first-principle dynamic model of the robot with a continuum arm.

A. Moving Mass Control-Based Design for Maneuverability and Robustness

The moving mass control has historically been overlooked in the design of robotic blimps. Previous designs in the literature often treated the non-negligible distance between the center of gravity (CG) and the center of buoyancy (CB) as a drawback and sought to mitigate its effects, such as swing-reducing control [34]. In contrast, we hypothesize that transforming this fixed distance into a variable facilitates attitude adjustment and is achievable through moving mass control.

This article proposes a unique robotic blimp design based on moving mass control. This design leverages the gravitational moment associated with the variable spatial distance between CG and CB to effectively control the attitude of a robotic blimp, especially during low-speed flight. Conventional control surfaces, such as the rudder, elevator, and aileron, commonly used in high-speed aerial vehicles such as fixed-wing aircraft, exhibit significantly reduced effectiveness in controlling low-speed robotic blimps. This limitation comes from the dependence of aerodynamic effects on dynamic pressure, e.g., $\|M\| \propto \rho V^2$, where M represents the aerodynamic moment, ρ represents air density, and V stands for the relative airspeed, equivalent to the cruising speed in calm environmental conditions.

To achieve moving mass control, we employ a lightweight continuum arm designed with two degrees of freedom (DoF) under the constant curvature assumption. More importantly, a bird-inspired end effector is mounted on the continuum arm, enabling object capture for resting or wind resistance, mimicking bird behavior.

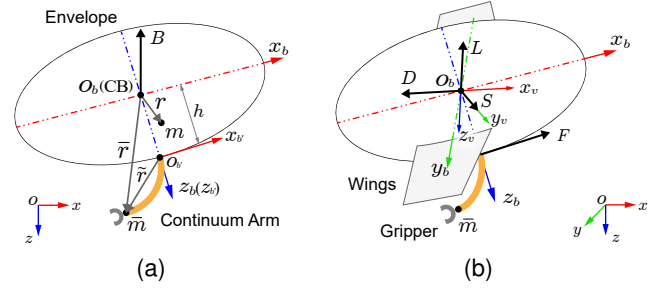


Fig. 2. Illustration of the RGLblimp-Q model with a continuum arm and two wings. (a) The mass distribution (side view), including the stationary mass m and the internal movable mass \tilde{m} . (b) The coordinate frames, thrust force from a propeller, and aerodynamic forces. The gripper is mounted on the end of the continuum arm, which will be discussed in Sec. IV-B.

B. Motion Dynamics Modeling of RGLblimp-Q

In this section, we derive the translational and rotational dynamics model of the RGLblimp-Q. The RGLblimp-Q is modeled as a rigid-body system, subject to inertial forces and moments exerted by the moving mass within the robot, as well as aerodynamic forces and moments arising from the surrounding airflow, as illustrated in Fig. 2. The actuation of the system comprises a continuum arm serving as an internal movable mass \tilde{m} for moving mass control, along with a propeller generating thrust F .

The dynamics model is conceptualized as a system of two point masses, as shown in Fig. 2a. The stationary mass, including wings and an envelope filled with helium, is denoted as m , characterized by a constant displacement r with respect to CB. The internal movable mass, represented by a continuum arm with a gripper, is denoted as \tilde{m} , featuring a controllable displacement \tilde{r} with respect to CB.

The coordinate frames and external forces are defined following the convention [50] and illustrated in Fig. 2b. The position and orientation of the robot are defined with respect to the earth-fixed inertial frame $O-xyz$. Motion, including the translational and rotational velocities of the RGLblimp-Q, is referenced to a body-fixed frame $O_b-x_b y_b z_b$, with its origin O_b defined at CB. The velocity reference frame $O_b-x_v y_v z_v$ is established to model aerodynamics, with its O_b-x_v axis aligned with the direction of the translational velocity of the robot. The subscripts b and i indicate that the items are expressed in the body-fixed frame and the earth-fixed inertial frame, respectively. The position vector $p_i = [x, y, z]^T$ describes the displacement of the origin of the inertial frame O with respect to the origin of the body-frame O_b . The Euler angles, including the roll angle ϕ , pitch angle θ , and yaw angle ψ , represent orientation, denoted as $e_i = [\phi, \theta, \psi]^T$. Let $v_b = [u, v, w]^T$ and $\omega_b = [p, q, r]^T$ represent the translational and rotational velocities expressed in the body-fixed frame, respectively. As commonly used in the literature [50], rotation from the body-frame to the inertial frame follows the roll-pitch-yaw (RPY)

sequence, i.e.,

$$\begin{aligned} \mathbf{R} &= \mathbf{R}_z(\psi)\mathbf{R}_y(\theta)\mathbf{R}_x(\phi) \\ &= \begin{bmatrix} c_\psi & -s_\psi & 0 \\ s_\psi & c_\psi & 0 \\ 0 & 0 & 1 \end{bmatrix} \begin{bmatrix} c_\theta & 0 & s_\theta \\ 0 & 1 & 0 \\ -s_\theta & 0 & c_\theta \end{bmatrix} \begin{bmatrix} 1 & 0 & 0 \\ 0 & c_\phi & -s_\phi \\ 0 & s_\phi & c_\phi \end{bmatrix} \\ &= \begin{bmatrix} c_\theta c_\psi & s_\phi s_\theta c_\psi - c_\phi s_\psi & c_\phi s_\theta c_\psi + s_\phi s_\psi \\ c_\theta s_\psi & s_\phi s_\theta s_\psi + c_\phi c_\psi & c_\phi s_\theta s_\psi - s_\phi c_\psi \\ -s_\theta & s_\phi c_\theta & c_\phi c_\theta \end{bmatrix}, \end{aligned} \quad (1)$$

where c_ϕ , s_ϕ , c_θ , s_θ , c_ψ , and s_ψ stand for $\cos(\phi)$, $\sin(\phi)$, $\cos(\theta)$, $\sin(\theta)$, $\cos(\psi)$, and $\sin(\psi)$, respectively.

The kinematics of the RGBlimp-Q are described by

$$\dot{\mathbf{p}}_i = \mathbf{R}\mathbf{v}_b, \quad (2)$$

$$\dot{\mathbf{e}}_i = \mathbf{P}\boldsymbol{\omega}_b. \quad (3)$$

Here, the changing rate of the Euler angles $\dot{\mathbf{e}}_i$ and the rotational velocity $\boldsymbol{\omega}_b$ are related through the transformation matrix based on the RPY sequence, i.e.,

$$\mathbf{P} = \begin{bmatrix} 1 & \sin\phi \tan\theta & \cos\phi \tan\theta \\ 0 & \cos\phi & -\sin\phi \\ 0 & \sin\phi \sec\theta & \cos\phi \sec\theta \end{bmatrix}. \quad (4)$$

The relationship between the time derivative of any given vector \mathbf{c} expressed in the inertial frame $\dot{\mathbf{c}}_i$ and that expressed in the body-fixed frame $\dot{\mathbf{c}}_b$ follows¹

$$\dot{\mathbf{c}}_i = \mathbf{R}(\dot{\mathbf{c}}_b + \boldsymbol{\omega}_b \times \mathbf{c}_b). \quad (5)$$

Based on Euler's first law of motion, the translational motion of the robot is described as

$$\mathbf{F}_b = m(\dot{\mathbf{v}}_b + \boldsymbol{\omega}_b \times \mathbf{v}_b + \mathbf{a}), \quad (6)$$

where \mathbf{a} stands for the sum of Euler and centripetal acceleration exerted by the point mass m due to the displacement \mathbf{r} , defined as

$$\mathbf{a} = \dot{\boldsymbol{\omega}}_b \times \mathbf{r} + \boldsymbol{\omega}_b \times (\boldsymbol{\omega}_b \times \mathbf{r}). \quad (7)$$

The term \mathbf{F}_b denotes the total external force acting on the stationary mass m of the RGBlimp-Q, calculated as

$$\mathbf{F}_b = F\mathbf{i}_b + (mg - B)\mathbf{R}^T\mathbf{k}_i + \mathbf{F}_{\text{aero}} + \mathbf{f}. \quad (8)$$

Here, F represents the thrust force from the propeller, aligned with the x_b axis as shown in Fig. 2. $\mathbf{i}_b = [1, 0, 0]^T$ and $\mathbf{k}_i = [0, 0, 1]^T$ are unit vectors along the $O_b x_b$ and Oz axis, respectively. g is the gravitational acceleration. $B = \rho g V_{\text{He}}$ represents the buoyant lift, where ρ is the density of air and V_{He} is the volume of helium gas. \mathbf{F}_{aero} denotes the aerodynamic forces acting on the robot expressed in the body-fixed frame.

The term \mathbf{f} represents the total force acting on the stationary mass, exerted by the internal movable mass, which includes gravity and equivalent force, i.e.,

$$\mathbf{f} = \bar{m}g\mathbf{R}^T\mathbf{k}_i - \bar{m}\dot{\mathbf{v}}. \quad (9)$$

¹Here $\dot{\mathbf{R}} = \mathbf{R}\boldsymbol{\omega}_b^\times$ is used for derivation, where $\boldsymbol{\omega}_b^\times$ is the skew-symmetric matrix corresponding to $\boldsymbol{\omega}_b$.

Here, $\dot{\mathbf{v}}$ denotes the time derivative of the velocity of the internal movable mass \bar{m} , expressed in the body-fixed frame, calculated as

$$\begin{aligned} \dot{\mathbf{v}} &= \mathbf{R}^T \frac{d\bar{\mathbf{v}}_i}{dt} = \mathbf{R}^T \frac{d}{dt} \mathbf{R}(\mathbf{v}_b + \bar{\mathbf{v}} + \boldsymbol{\omega}_b \times \bar{\mathbf{r}}) \\ &= \dot{\mathbf{v}}_b + \boldsymbol{\omega}_b \times \mathbf{v}_b + \dot{\bar{\mathbf{v}}} + 2\boldsymbol{\omega}_b \times \bar{\mathbf{v}} \\ &\quad + \dot{\boldsymbol{\omega}}_b \times \bar{\mathbf{r}} + \boldsymbol{\omega}_b \times (\boldsymbol{\omega}_b \times \bar{\mathbf{r}}), \end{aligned} \quad (10)$$

where $\bar{\mathbf{v}} = \dot{\bar{\mathbf{r}}}$ represents the time derivative of the displacement vector from O_b to the CG of the movable mass \bar{m} , i.e., $\bar{\mathbf{r}}$.

Based on Euler's second law of motion, the rotational motion of the robot is described as

$$\mathbf{T}_b = \mathbf{I}\dot{\boldsymbol{\omega}}_b + \boldsymbol{\omega}_b \times (\mathbf{I}\boldsymbol{\omega}_b) + m\mathbf{r} \times (\dot{\mathbf{v}}_b + \boldsymbol{\omega}_b \times \mathbf{v}_b). \quad (11)$$

Here, \mathbf{I} represents the inertia matrix of the stationary mass about the origin of the body-fixed frame. The total external moment \mathbf{T}_b is calculated as

$$\mathbf{T}_b = Fh\mathbf{j}_b + \mathbf{r} \times mg\mathbf{R}^T\mathbf{k} + \mathbf{T}_{\text{aero}} + \bar{\mathbf{r}} \times \mathbf{f}. \quad (12)$$

Here, h denotes the distance between the thrust force F and the $O_b x_b$ axis, as depicted in Fig. 2. $\mathbf{j}_b = [0, 1, 0]^T$ represents the unit vector along the $O_b y_b$ axis. \mathbf{T}_{aero} denotes the aerodynamic moment acting on the robot, expressed in the body-fixed frame.

Let $\bar{\mathbf{F}} = [\bar{F}_x, \bar{F}_y, \bar{F}_z]^T = \dot{\bar{\mathbf{v}}} = \ddot{\bar{\mathbf{r}}}$ represent the second derivative of the displacement vector $\bar{\mathbf{r}}$ with respect to time. Combining Eqs. (6)-(12), the motion dynamics of the robot is expressed in terms of the inputs $F, \bar{F}_x, \bar{F}_y, \bar{F}_z$ in a vector form, i.e.,

$$\mathbf{E} \begin{bmatrix} \dot{\mathbf{v}}_b \\ \dot{\boldsymbol{\omega}}_b \\ \dot{\bar{\mathbf{v}}} \end{bmatrix} = \begin{bmatrix} \bar{\mathbf{F}} \\ \bar{\mathbf{T}} \\ \mathbf{0}_{3 \times 1} \end{bmatrix} + \mathbf{N} \begin{bmatrix} F \\ \bar{\mathbf{F}} \end{bmatrix}, \quad (13)$$

where

$$\begin{aligned} \bar{\mathbf{F}} &= (m + \bar{m})\mathbf{v}_b \times \boldsymbol{\omega}_b + (\boldsymbol{\omega}_b \times \mathbf{l}_g) \times \boldsymbol{\omega}_b + \\ &\quad (mg + \bar{m}g - B)\mathbf{R}^T\mathbf{k} + \mathbf{F}_{\text{aero}} + 2\bar{m}\bar{\mathbf{v}} \times \boldsymbol{\omega}_b, \end{aligned} \quad (14)$$

$$\begin{aligned} \bar{\mathbf{T}} &= \mathbf{l}_g \times (\mathbf{v}_b \times \boldsymbol{\omega}_b) + (\mathbf{I} - \bar{m}(\bar{\mathbf{r}}^\times)^2)\boldsymbol{\omega}_b \times \boldsymbol{\omega}_b + \\ &\quad \mathbf{l}_g \times g\mathbf{R}^T\mathbf{k} + \mathbf{T}_{\text{aero}} + 2\bar{m}\bar{\mathbf{r}} \times (\bar{\mathbf{v}} \times \boldsymbol{\omega}_b), \end{aligned} \quad (15)$$

$$\mathbf{E} = \begin{bmatrix} (m + \bar{m})\mathbf{1}_3 & -\mathbf{l}_g^\times & \bar{m}\mathbf{1}_3 \\ \mathbf{l}_g^\times & \mathbf{I} - \bar{m}(\bar{\mathbf{r}}^\times)^2 & \bar{m}\bar{\mathbf{r}}^\times \\ \mathbf{0}_3 & \mathbf{0}_3 & \mathbf{1}_3 \end{bmatrix}, \quad (16)$$

$$\mathbf{N} = \begin{bmatrix} \mathbf{i}_b & h\mathbf{j}_b & \mathbf{0}_{1 \times 3} \\ \mathbf{0}_{3 \times 2} & \mathbf{1}_3 \end{bmatrix}^T. \quad (17)$$

Here, $\mathbf{l}_g = m\mathbf{r} + \bar{m}\bar{\mathbf{r}} = (m + \bar{m})\mathbf{r}_g$ where \mathbf{r}_g denotes the overall CG of the system of two point masses. $\mathbf{0}$ represents the zero vector or matrix. $\mathbf{1}_3$ represents the identity matrix.

Additionally, the aerodynamics terms in Eqs. (14) and (15) need to be considered. Without loss of generality, we assume a windless environment, focusing on motion-induced aerodynamics. The transformation from the velocity reference frame $O_b - x_v y_v z_v$ to the body-fixed frame $O_b - x_b y_b z_b$ is expressed as

$$\mathbf{R}_v^b = \begin{bmatrix} \cos\alpha \cos\beta & -\cos\alpha \sin\beta & -\sin\alpha \\ \sin\beta & \cos\beta & 0 \\ \sin\alpha \cos\beta & -\sin\alpha \sin\beta & \cos\alpha \end{bmatrix}. \quad (18)$$

Here, $\alpha = \arctan(w/u)$ represents the angle of attack, and $\beta = \arcsin(v/V)$ denotes the sideslip angle, where $V = \|\mathbf{v}_b\|$ represents the velocity magnitude.

As illustrated in Fig. 2b, the aerodynamic forces, including the drag force D , the side force S , and the lift force L , are defined in the velocity reference frame. Similarly, the aerodynamic moments comprise the roll moment M_x , the pitch moment M_y , and the yaw moment M_z . The aerodynamic forces and moments are described as

$$\mathbf{F}_{\text{aero}} = \mathbf{R}_v^b [-D, S, -L]^T, \quad (19)$$

$$\mathbf{T}_{\text{aero}} = \mathbf{R}_v^b [M_x, M_y, M_z]^T. \quad (20)$$

Following the literature, we model the aerodynamic forces and moments as functions of the angle of attack α , the sideslip angle β , and the velocity magnitude V , i.e.,

$$D = 1/2 \rho V^2 A C_D(\alpha, \beta), \quad (21)$$

$$S = 1/2 \rho V^2 A C_S(\alpha, \beta), \quad (22)$$

$$L = 1/2 \rho V^2 A C_L(\alpha, \beta), \quad (23)$$

$$M_x = 1/2 \rho V^2 A C_{M_x}(\alpha, \beta) + K_x p, \quad (24)$$

$$M_y = 1/2 \rho V^2 A C_{M_y}(\alpha, \beta) + K_y q, \quad (25)$$

$$M_z = 1/2 \rho V^2 A C_{M_z}(\alpha, \beta) + K_z r. \quad (26)$$

Here, A represents the reference area, characterizing the geometric design of the robot. The terms in the form of C_{\square} represent constant aerodynamic coefficients. Additionally, K_x , K_y , and K_z , all negative, denote the rotational damping coefficients.

C. Design and Kinematics of the Continuum Arm

This section introduces the kinematics of the continuum arm without twist, based on the assumption of constant curvature (CC). Furthermore, we simplify the continuum arm with a lightweight and fixed-length backbone (the central axis), thus a point mass \tilde{m} on the end of the arm is considered, which is moving on a manifold with 2 DoF.

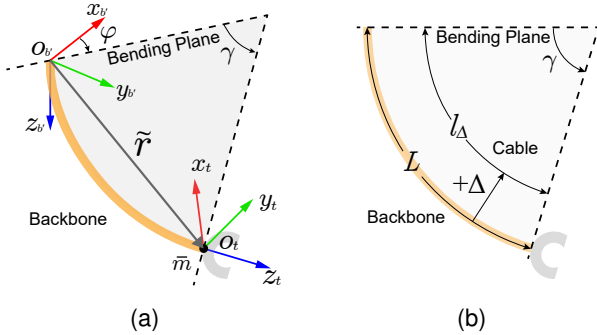


Fig. 3. The geometric illustration of the continuum arm moving in three dimensions. (a) shows the arm bending in a plane, with reference frames and angle parameters. The view (b) is normal to the bending plane, depicting a cable at a distance $+\Delta$ from the backbone along the direction of radius.

Figure 3 illustrates the CC model, where the continuum arm is approximated as a continuous segment with curvature constant in space but varying in time. The base frame of the continuum arm $O_{b'}-x_{b'}y_{b'}z_{b'}$ has the same orientation with the body-fixed frame $O_b-x_b y_b z_b$, but translated along O_b-z_b

axis with a distance h , as shown in Fig. 2a. The tool frame of the continuum arm $O_t-x_t y_t z_t$ is established on the end of the continuum arm. Under the CC assumption, the kinematic homogeneous transformation matrix $\mathbf{C}_{b'}^t \in \text{SE}(3)$ maps arm $O_{b'}-x_{b'}y_{b'}z_{b'}$ into $O_t-x_t y_t z_t$, given by

$$\mathbf{C}_{b'}^t(\gamma, \varphi) = \mathbf{R}_z(\varphi) \begin{bmatrix} \mathbf{R}_x(\gamma) & \frac{L}{\gamma} \begin{bmatrix} \cos(\gamma)-1 \\ \sin(\gamma) \\ 0 \end{bmatrix} \\ 0 & 1 \end{bmatrix} \mathbf{R}_z(-\varphi). \quad (27)$$

Here, L is the constant length of backbone of the continuum arm. The angle $\varphi \in [0, 2\pi)$ and $\gamma \in [0, \pi/2]$ stand for the direction of bending and the angle of curvature, respectively, as shown in Fig. 3. The rotation matrices \mathbf{R}_x and \mathbf{R}_z are given in Eq. (1).

We examine the translation vector from $O_{b'}-x_{b'}y_{b'}z_{b'}$ to $O_t-x_t y_t z_t$, denoted as $\tilde{\mathbf{r}}$. This translation vector plays a crucial role in the moving mass control of the RGBlimp-Q. Derived from transformation matrix (27), the expression for $\tilde{\mathbf{r}}$ is given by

$$\tilde{\mathbf{r}} = \frac{L}{\gamma} \begin{bmatrix} \cos \varphi (1 - \cos \gamma) \\ \sin \varphi (1 - \cos \gamma) \\ \sin \gamma \end{bmatrix}. \quad (28)$$

The configuration $[\gamma, \varphi]^T \in \mathbb{R}^2$ is a standard angle parametrization widely used in continuum robot studies. However, this angle-based approach presents challenges such as singularities (when $\gamma = 0$). To address these issues, Santana and Rus proposed a novel q -parametrization [47]. This method describes the kinematics of a CC segment based on the lengths of four uniformly distributed cables aligned parallel to the backbone, which is well-suited for cable-driven design. To address the demands of lightweight design and spatial motion, we consider three cables in the q -parametrization.

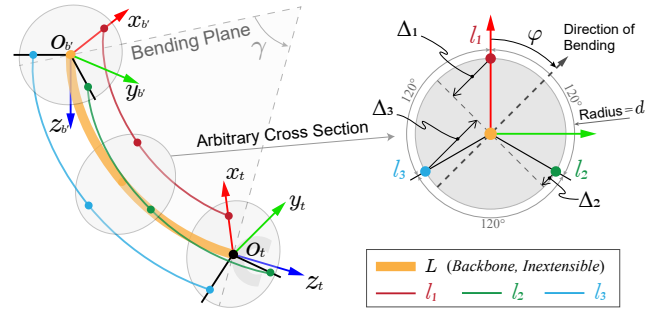


Fig. 4. Illustration for the q -parametrization of the continuum arm. The parameters q are defined as a linear combination of the lengths of the uniformly-distributed three cables. The geometric relation in any cross section is shown in right side of this figure, which presents the cables connected with no twist and same distance d from the center.

Figure 4 illustrates the q -parametrization of the continuum arm, featuring three uniformly distributed cables l_1 , l_2 , and l_3 aligned parallel to the backbone in the bending plane of the continuum arm. These cables share the same curvature as the backbone, maintaining a constant distance d from the center in arbitrary cross section of the continuum arm, as shown in the right plot of Fig. 4. Trigonometric considerations allow us to

derive the projection distances on the bending plane Δ_i ($i = 1, 2, 3$) of the constant distance d for each cable, i.e.,

$$\begin{aligned}\Delta_1 &= +d \cos \varphi, \\ \Delta_2 &= -d \sin\left(\frac{\pi}{6} - \varphi\right), \\ \Delta_3 &= -d \sin\left(\frac{\pi}{6} + \varphi\right).\end{aligned}\quad (29)$$

Furthermore, the length of cable i with the projection distance Δ_i , as shown in Fig. 3b, is calculated by

$$l_i = L - \gamma \Delta_i, \quad (i = 1, 2, 3). \quad (30)$$

Combining Eqs. (29) and (30) yields the lengths of the three cables as function of γ and φ , i.e.,

$$\begin{aligned}l_1(\gamma, \varphi) &= L - d\gamma \cos \varphi, \\ l_2(\gamma, \varphi) &= L + d\gamma \sin\left(\frac{\pi}{6} - \varphi\right), \\ l_3(\gamma, \varphi) &= L + d\gamma \sin\left(\frac{\pi}{6} + \varphi\right).\end{aligned}\quad (31)$$

Based on the cable length calculations, we define the new state configuration as

$$\begin{aligned}\delta_x &= \frac{1}{3}(l_2 + l_3 - 2l_1) = d\gamma \cos \varphi, \\ \delta_y &= \frac{\sqrt{3}}{3}(l_3 - l_2) = d\gamma \sin \varphi, \\ \delta &= \sqrt{\delta_x^2 + \delta_y^2} = d\gamma.\end{aligned}\quad (32)$$

Note that, δ_x and δ_y describe the bending degree of the continuum in the x_b and y_b directions, respectively.

Let $q = [\delta_x, \delta_y]^T \in \mathbb{R}^2$ represent the q -parametrization. The mapping from the q -parametrization to the angle parametrization is described as

$$\varphi = \arccos\left(\frac{\delta_x}{\delta}\right) = \arcsin\left(\frac{\delta_y}{\delta}\right), \quad (33)$$

$$\gamma = \frac{\delta}{d}. \quad (34)$$

Let the velocity in q -parametrization serve as the control input, denoted as $\dot{\delta}_x$ and $\dot{\delta}_y$. Such input is well-suited for a cable-driven continuum arm, discussed in detail in Sec. IV-A. Combining Eqs. (28), (33), and (34), the translation vector $\tilde{\mathbf{r}}$ in the q -parametrization is given by

$$\tilde{\mathbf{r}} = \frac{Ld}{\delta^2} \begin{bmatrix} \delta_x(1 - \cos \frac{\delta}{d}) \\ \delta_y(1 - \cos \frac{\delta}{d}) \\ \delta \sin \frac{\delta}{d} \end{bmatrix}. \quad (35)$$

Therefore, the displacement vector from the origin of the body-fixed frame O_b to the tool frame O_t , i.e., $\tilde{\mathbf{r}}$, is calculated as $\tilde{\mathbf{r}} = [0, 0, h]^T + \tilde{\mathbf{r}}$. Furthermore, the time derivative of the displacement vector $\tilde{\mathbf{r}}$ is determined as

$$\dot{\tilde{\mathbf{r}}} = \mathbf{J}_{3 \times 2} \begin{bmatrix} \dot{\delta}_x \\ \dot{\delta}_y \end{bmatrix}, \quad (36)$$

where $\mathbf{J}_{3 \times 2}$ denotes the Jacobian of the RHS of Eq. (35).

D. Full Dynamic Model of RGBlimp-Q

Combining the motion dynamics (13) and the kinematics of the continuum arm (36), we derive the full dynamic model of the RGBlimp-Q, expressed in terms of the system states $\mathbf{p}_i, \mathbf{e}_i, \mathbf{v}_b, \boldsymbol{\omega}_b, \tilde{\mathbf{r}}$ and the control inputs $F, \dot{\delta}_x, \dot{\delta}_y$, i.e.,

$$\begin{bmatrix} \dot{\mathbf{p}} \\ \dot{\mathbf{e}} \\ \dot{\tilde{\mathbf{r}}} \\ \dot{\mathbf{v}}_b \\ \dot{\boldsymbol{\omega}}_b \end{bmatrix} = \begin{bmatrix} \mathbf{R}\mathbf{v}_b \\ \mathbf{P}\boldsymbol{\omega}_b \\ \mathbf{0}_{3 \times 1} \\ \mathbf{A} \begin{bmatrix} \tilde{\mathbf{f}} \\ \tilde{\mathbf{t}} \end{bmatrix} \end{bmatrix} + \mathbf{B} \begin{bmatrix} F \\ \dot{\delta}_x \\ \dot{\delta}_y \end{bmatrix}, \quad (37)$$

where

$$\begin{aligned}\tilde{\mathbf{f}} &= (m + \bar{m})\mathbf{v}_b \times \boldsymbol{\omega}_b + (\boldsymbol{\omega}_b \times \mathbf{l}_g) \times \boldsymbol{\omega}_b + \\ &\quad (mg + \bar{m}g - B)\mathbf{R}^T \mathbf{k} + \mathbf{F}_{\text{aero}},\end{aligned}\quad (38)$$

$$\begin{aligned}\tilde{\mathbf{t}} &= \mathbf{l}_g \times (\mathbf{v}_b \times \boldsymbol{\omega}_b) + (\mathbf{I} - \bar{m}(\bar{\mathbf{r}}^\times)^2) \boldsymbol{\omega}_b \times \boldsymbol{\omega}_b + \\ &\quad \mathbf{l}_g \times g\mathbf{R}^T \mathbf{k} + \mathbf{T}_{\text{aero}},\end{aligned}\quad (39)$$

$$\mathbf{A} = \begin{bmatrix} (m + \bar{m})\mathbf{1}_3 & -\mathbf{l}_g^\times \\ \mathbf{l}_g^\times & \mathbf{I} - \bar{m}(\bar{\mathbf{r}}^\times)^2 \end{bmatrix}^{-1}, \quad (40)$$

$$\mathbf{B} = \begin{bmatrix} \mathbf{0}_{6 \times 4} & & & \\ & \mathbf{0}_{3 \times 1} & \mathbf{1}_3 & \\ \mathbf{A} \begin{bmatrix} \mathbf{i}_b & -2\bar{m}\boldsymbol{\omega}^\times \\ h\mathbf{j}_b & -2\bar{m}\bar{\mathbf{r}}^\times \boldsymbol{\omega}^\times \end{bmatrix} & & & \end{bmatrix} \begin{bmatrix} 1 & \mathbf{0}_{1 \times 2} \\ \mathbf{0}_{3 \times 1} & \mathbf{J}_{3 \times 2} \end{bmatrix}. \quad (41)$$

Here, the determinant of \mathbf{A} is always nonzero, ensuring that \mathbf{A}^{-1} is always well-defined.

We now delve into the steady-state equations governing the equilibria of the robot dynamics. Assuming a fixed thrust force F and a constant moving mass displacement vector $\tilde{\mathbf{r}}$, the steady-state equations are derived by setting the time derivatives of Eq. (36) to zero, yielding

$$\begin{aligned}0 &= \mathbf{F}_{\text{aero}} + (m + \bar{m})\mathbf{v}_b \times \boldsymbol{\omega}_b + (\boldsymbol{\omega}_b \times \mathbf{l}_g) \times \boldsymbol{\omega}_b + \\ &\quad (mg + \bar{m}g - B)\mathbf{R}^T \mathbf{k} + F\mathbf{i}_b,\end{aligned}\quad (42)$$

$$\begin{aligned}0 &= \mathbf{T}_{\text{aero}} + \mathbf{l}_g \times (\mathbf{v}_b \times \boldsymbol{\omega}_b) + (\mathbf{I} - \bar{m}(\bar{\mathbf{r}}^\times)^2) \boldsymbol{\omega}_b \times \boldsymbol{\omega}_b + \\ &\quad \mathbf{l}_g \times g\mathbf{R}^T \mathbf{k} + Fh\mathbf{j}_b.\end{aligned}\quad (43)$$

The solution to these equations provides the steady-state motion of the robot, which is instrumental in the subsequent aerodynamic parameter identification outlined in Sec. V-C.

IV. CONTINUUM ARM SYSTEM

In this section, we present the design of a mechanically decoupled cable-driven continuum arm tailored for the moving mass control of the RGBlimp-Q. This design adheres to the CC assumption and emphasizes attributes such as lightweight and agile motion, making it well-suited for a payload-limited miniature aircraft like the RGBlimp-Q.

A. Mechanically Decoupled Cable-Driven Design

In our design, we consider the continuum arm without twist under the CC assumption, as discussed in Sec. III-C and illustrated in Fig. 4, where the cables are treated as the driving cables. To achieve spatial motion of the continuum

arm, a minimum of three cables is required. These cables are constrained by the backbone, resulting in a two-degree-of-freedom motion described in terms of either (γ, φ) or (δ_x, δ_y) . In the literature [39], these cables are typically controlled by independent actuators (motors) within specific constraints. However, such redundancy in motors leads to increased inefficiency in load handling, a concern that is particularly pertinent in the design of miniature aircrafts such as the RGBlimp-Q. To mitigate this inefficiency, we utilize a compound gear train mechanism to achieve decoupling for the cable-driven continuum arm. This approach ensures that the two-degree-of-freedom motion of the robot are independently controlled by two corresponding actuators.

Let's reconsider the relation between the lengths of three cables (l_1, l_2, l_3) and the configuration in the q -parametrization (δ_x, δ_y) . Combining Eqs. (31) and (32), we derive the lengths of the three cables as functions of δ_x and δ_y , i.e.,

$$\begin{bmatrix} l_1 \\ l_2 \\ l_3 \end{bmatrix} = \begin{bmatrix} -1 & 0 \\ 1 & -\frac{\sqrt{3}}{2} \\ 1 & \frac{\sqrt{3}}{2} \end{bmatrix} \begin{bmatrix} \delta_x \\ \delta_y \end{bmatrix}. \quad (44)$$

These equations illustrate that the lengths of the three cables are linearly dependent, i.e., $l_1 + l_2 + l_3 = 0$. Further, it is observed that the length l_1 is independent of δ_y but decreases with δ_x . Meanwhile, l_2 and l_3 increase with $\frac{1}{2}\delta_x$. The length l_2 decreases with $\frac{\sqrt{3}}{2}\delta_y$, while l_3 increases with $\frac{\sqrt{3}}{2}\delta_y$.

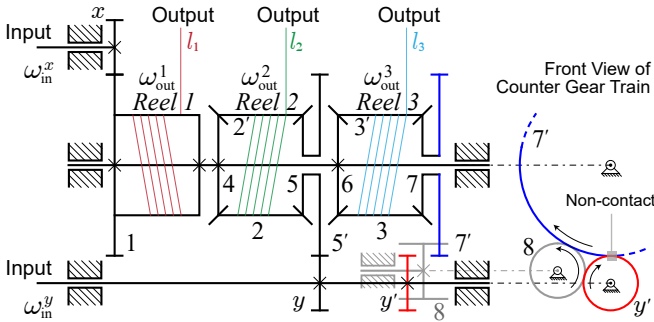


Fig. 5. Representation of the proposed compound-gear-train-based decoupling mechanism. The design ensures independent control for the 2 DoF of the continuum arm by two actuators accordingly. The three cables are wound at each of three outputting reels, including differential-based reels 2 and 3, and the fixed-axis reel 1 with an opposite winding direction. The left part of the figure shows the main structure of the mechanism in the side view. The right part depicted the front view of the counter gear, i.e., gear 8, whose rotating axis is in a different plane. Note that the gear 7' (blue) and y' (red) are not engaged, as shown in the side view.

Based on Eq. (44), we propose the mechanism of a compound gear train for decoupled cable driving, as shown in Fig.5. The mechanism uses two actuators for decoupled inputs, yielding three rotary motions for winding the three cables under the constraint in Eq. (44) accordingly. The inputs and outputs of the mechanism are defined as the rotational speeds of the two actuators and the three reels, respectively, denoted as $(\omega_{in}^x, \omega_{in}^y)$ and $(\omega_{out}^1, \omega_{out}^2, \omega_{out}^3)$. Specifically, reel 1 is directly affixed to a shaft, i.e., the fixed-axis reel, while the reel 2 and reel 3 are made of differential gear train, i.e., differential-based reels. The setup includes seven spur gears ($x, y, y', 1, 5', 7', 8$) and eight bevel gears (2, 2', 3, 3', 4, 5, 6, 7). To determine the

overall drive ratio R of the compound gear train, we examine the rotational speeds ω and tooth numbers N of each gear. Beginning with the fixed-axis gear train segment, we compute the rotational speed of reel 1 as

$$\omega_{out}^1 = R_x^1 \omega_{in}^x = -\frac{N_x}{N_1} \omega_{in}^x. \quad (45)$$

Here, R_x^1 represents the drive ratio from gear x to gear 1, with the negative sign indicating the opposite direction of rotation. In addition, gear 4 and gear 6 are fixed on the same shaft with gear 1, resulting in $\omega_4 = \omega_6 = \omega_1$. Similarly, we obtain

$$\omega_5 = \omega_{5'} = -\frac{N_y}{N_{5'}} \omega_{in}^y, \quad \omega_7 = \omega_{7'} = \frac{N_8}{N_{7'}} \frac{N_{y'}}{N_8} \omega_{in}^y. \quad (46)$$

The tooth numbers of bevel gears in the differential gear train are designed the same, i.e., $N_4 = N_5 = N_6 = N_7$. Furthermore, we take the rotation relative to the the moving axis (i.e., the rotation axes of reels 2 and 3) into account, yielding

$$\begin{aligned} \frac{\omega_4 - \omega_{out}^2}{\omega_5 - \omega_{out}^2} &= -\frac{N_5}{N_4} = -1, \\ \frac{\omega_6 - \omega_{out}^3}{\omega_7 - \omega_{out}^3} &= -\frac{N_7}{N_6} = -1. \end{aligned} \quad (47)$$

The rotational speeds of reels 2 and 3 are then calculated as

$$\omega_{out}^2 = \frac{\omega_4 + \omega_5}{2}, \quad \omega_{out}^3 = \frac{\omega_6 + \omega_7}{2}. \quad (48)$$

Combining Eqs. (45), (46) and (48), we obtain the rotational speeds of reels 2 and 3 as

$$\begin{aligned} \omega_{out}^2 &= -\frac{1}{2} \frac{N_x}{N_1} \omega_{in}^x - \frac{1}{2} \frac{N_y}{N_{5'}} \omega_{in}^y, \\ \omega_{out}^3 &= -\frac{1}{2} \frac{N_x}{N_1} \omega_{in}^x + \frac{1}{2} \frac{N_{y'}}{N_{7'}} \omega_{in}^y. \end{aligned} \quad (49)$$

Here, we selected two different sets of tooth numbers for the spur gears i.e., $N_x = N_y = N_{y'} = N_8$ and $N_1 = N_{5'} = N_{7'}$. Denoting the drive ratio in Eqs. (45) and (49) as $k = \frac{N_x}{N_1} = \frac{N_y}{N_{5'}} = \frac{N_{y'}}{N_{7'}}$, we obtain

$$\begin{aligned} \omega_{out}^1 &= -k \omega_{in}^x, \\ \omega_{out}^2 &= -\frac{1}{2} k \omega_{in}^x - \frac{1}{2} k \omega_{in}^y, \\ \omega_{out}^3 &= -\frac{1}{2} k \omega_{in}^x + \frac{1}{2} k \omega_{in}^y. \end{aligned} \quad (50)$$

Considering that cable l_1 is wound in the opposite direction to l_2 and l_3 , and the radii of the reels are designed the same, denoted as r_{reel} , the velocities of the cables are then calculated as

$$\begin{bmatrix} \dot{l}_1 \\ \dot{l}_2 \\ \dot{l}_3 \end{bmatrix} = \begin{bmatrix} -1 & 0 \\ 1 & -\frac{\sqrt{3}}{2} \\ 1 & \frac{\sqrt{3}}{2} \end{bmatrix} \begin{bmatrix} k r_{reel} \omega_{in}^x \\ \frac{\sqrt{3}}{3} k r_{reel} \omega_{in}^y \end{bmatrix}. \quad (51)$$

Comparing Eqs. (44) and (51), we find

$$\dot{\delta}_x = k r_{reel} \omega_{in}^x, \quad \dot{\delta}_y = \frac{\sqrt{3}}{3} k r_{reel} \omega_{in}^y. \quad (52)$$

By considering $(\omega_{in}^x, \omega_{in}^y)$ as inputs, the decoupled cable-driven mechanism facilitates independent control of the 2-DoF continuum arm using two actuators, thereby mitigating complexity of controlling the three cables.

B. A Bionic Bird's Claw for Resisting Wind

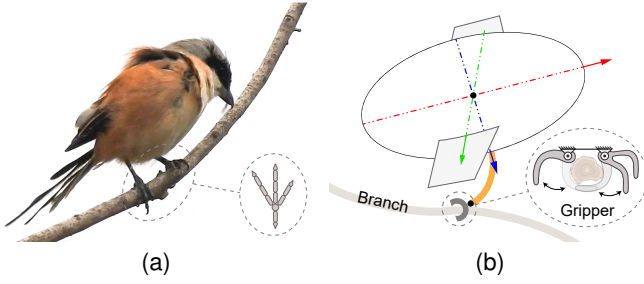


Fig. 6. The gripper is a bird-inspired robotic effector mounted at the end of the continuum arm, which enables robotic blimps to catch objects for resting or resisting wind. (a) Birds use their claws, usually anisodactyl, to grasp branch securely and to anchor the body in a windy environment [33]. (b) The RGBlimp-Q adopts the same strategy to resist environmental wind with its gripper open for standing and closed for holding a branch.

With their claws, birds effortlessly grasp and perch on trees, especially in windy conditions, as illustrated in Fig. 6. In contrast, current robotic blimps lack such an adaptive

mechanism to withstand wind disturbances.

Although robotic blimps feature durability, safety, and low noise levels compared to other aerial robots, they suffer from the long-standing challenge of wind disturbance, limiting their outdoor applications. In this work, we propose to leverage a bio-inspired claw mechanism, mimicking birds' behaviors, to address this challenge.

The bio-inspired claw is a lightweight robotic gripper mounted at the end of the continuum arm, resembling the structure of an anisodactyl bird, with its first toe pointing backwards and the remaining toes forward. This bionic claw is designed to reliably grasp a branch when closed. Additionally, the buoyancy and gravity of the RGBlimp-Q ensure that its attitude remains stable whether the claw is open or closed.

V. PROTOTYPE AND EXPERIMENTAL SETUP

The design proposed in Sec. III and Sec. IV is validated through the development of a prototype of RGBlimp-Q. In this section, we provide a detailed overview of the prototype, outlining its model parameters identified from a collection

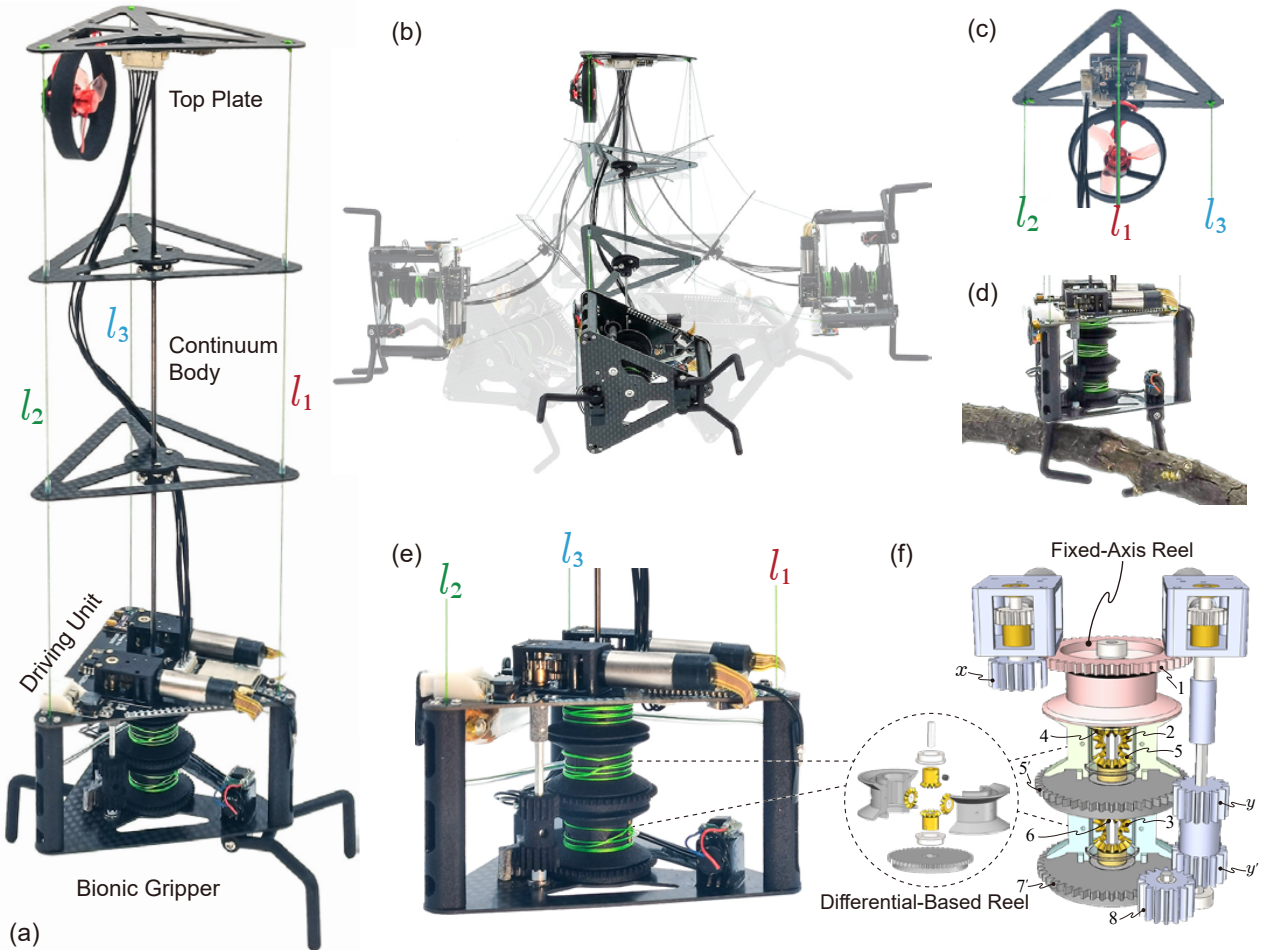


Fig. 7. Prototype of the continuum arm. (a) Four main parts make up the continuum arm, including the top plate, the continuum body, the driving unit, and the bionic gripper. (b) The spatial motion of the continuum arm is 2 DoF, which is constrained by the continuum body and driven by three cables. (c) The top plate includes a propeller and an IMU, whose circuit board and carbon fiber plate are connected to the driving unit by wires and cables, respectively. (d) The bionic gripper of the prototype holds a branch for resting or resisting wind. (e) The driving unit controls the continuum arm, the propeller and the bionic gripper based on sensor feedback, accounting for the main weight, i.e., ~ 65 g (80% total). (f) The gear box is composed of one fixed-axis reel, two differential-based reels, two motors with worm gear reducers, and gears of the same tooth number as designed in Sec. IV-A.

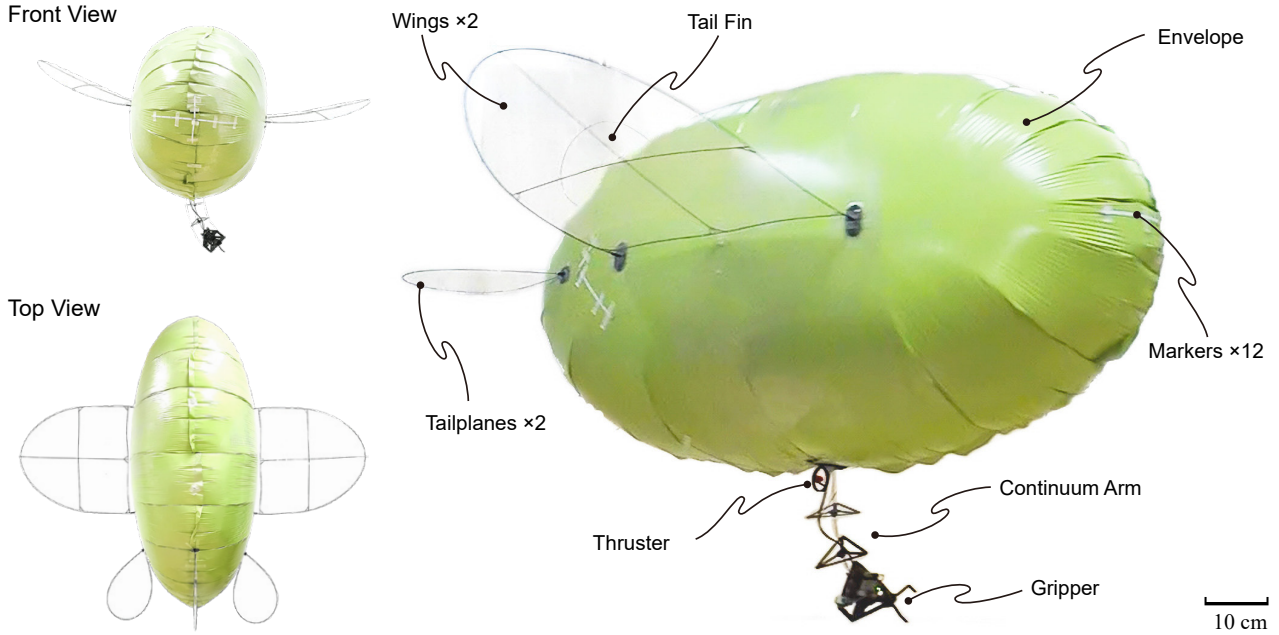


Fig. 8. The RGBlimp-Q prototype includes an envelope, a pair of main wings, a tail fin, two tailplanes, and the continuum arm with a battery. The left parts show the prototype in front view and top view. The components of the prototype are shown in the right part, which is a snapshot from a flight trial of the RGBlimp-Q prototype.

of open-loop steady flight data. Additionally, we introduce a classic proportional-integral-derivative (PID) controller, leveraging two inertial measurement units (IMUs) to achieve the desired flight performance – enhanced maneuverability and robustness. The experimental results are detailed in Sec. VI.

A. Continuum Arm Prototype

Following the design of the continuum arm, we have successfully developed a prototype, as shown in Fig. 7. The computer-aided design (CAD) models have been made available as open source on GitHub (<https://rgblimp.github.io>). The weight of the continuum arm is 81.79 g, excluding batteries, and it has a total length of 0.4 m with a backbone measuring 0.3 m made by Nickel-Titanium alloy.

The continuum arm comprises four main components, arranged from top to bottom, as illustrated in Fig. 7(a). At the top plate, a propeller and an IMU are mounted, serving propulsion and sensing functions, respectively. This plate also acts as a connector to the envelope of RGBlimp-Q. Below, the continuum body consists of two support plates and the backbone, ensuring the arm’s motion adheres to the constant curvature assumption. The driving box houses the gear box for the decoupled cable-driven mechanism, two motors, a control unit and another IMU. The decoupled mechanism is detailed in the CAD model, featuring one fixed-axis reel and two differential-based reels. Finally, the bionic gripper is affixed to the bottom of the continuum arm for standing or grasping objects, as illustrated in Fig. 7(d). It is worth noting that the driving cables wind in opposite directions between the fixed-axis reel and the two differential-based reels. Furthermore, these cables are guided from a horizontal to a vertical orientation through Teflon tubes, facilitating the movement of the continuum arm.

The propeller, with a diameter of 31 mm, is powered by a brushless DC (BLDC) motor *SE0802-KV19000* and an electronic speed controller (ESC) to regulate its speed effectively. Driving the system is a low-cost microcontroller *ESP32*, leveraging the *rosserial_arduino* library to establish a *Robot Operating System* (ROS) node, facilitating wireless network communication with a host computer.

B. RGBlimp-Q Prototype

A prototype of the RGBlimp-Q is developed, combining the continuum arm (acting as the moving mass \bar{m}) and the stationary mass m , encompassing an envelope, wings, and motion capture markers, as illustrated in Fig. 8. The mass distribution of the RGBlimp-Q prototype is detailed in Table I.

TABLE I
MASS DISTRIBUTION OF THE RGBLIMP-Q PROTOTYPE.

Component	Weight
Buoyant Lift^a $-B$ (Helium)	-194.23 gf
Stationary Mass m	108.69 g
Helium	26.93 g
Envelop	53.74 g
Main Wings	8.33 g $\times 2$
Tail Wings (Tail Fin & Tailplanes)	2.79 g $\times 3$
Motion Capture Markers (Infrared LEDs)	2.98 g
Moving Mass \bar{m}	92.21 g
Battery	10.42 g
Continuum Arm	81.79 g
Total Weight (Net^b)	6.67 g

^aThe total buoyancy from helium in gram force (gf). ^bThe total net weight stands for the weight remaining after deducting buoyancy, i.e., $m + \bar{m} - B$.

The envelope consists of an ellipsoidal mylar balloon filled with approximately 160 liters of helium, providing a total buoyant lift of 194.23 gf. The main wings and tail wings, which include a tail fin and two tailplanes, contribute to both aerodynamic lift and attitude stability. The main wings, similar to those in our previous work [7], feature a 400 mm wingspan and a 15 deg dihedral angle, adopting an aerodynamic shape. The tail fin is mounted vertically on the tail section of the envelope, while the pair of tailplanes are mounted horizontally. The motion capture markers, comprising 850 nm infrared LEDs, facilitate indoor motion capture experiments.

C. Experimental Setup and System Identification

The flight performance of the RGBlimp-Q prototype is evaluated through numerous flight trials conducted in both indoor and outdoor settings.

Indoor flights take place within a motion capture arena measuring $L10.0 \times W6.0 \times H3.0$ m, equipped with ten *Opti-Track* cameras. These cameras capture data at 60 Hz with an accuracy of 0.8 mm RMS in position estimation error. For outdoor flights, a side-view camera and an overhead camera, positioned 7 m above the ground, are used to record flight trajectories. Each trial, whether indoor or outdoor, utilizes an electromagnetic releaser to ensure stability and consistency in the starting pose. Communication between the robot and the host PC occurs via a router and ROS.

Utilizing the identification approach introduced in our previous work [7], the parameters in Eq. (37) are identified. The gravitational constant is set to $g = 9.81 \text{ m/s}^2$. The inertia tensor is calculated from the CAD model, yielding $\mathbf{I} = \text{diag}(0.035, 0.020, 0.015) \text{ kg} \cdot \text{m}^2$. The results of aerodynamic identification are presented as follows,

$$C_D(\alpha, \beta) = C_D^0 + C_D^\alpha \alpha^2 + C_D^\beta \beta^2, \quad (53)$$

$$C_S(\alpha, \beta) = C_S^0 + C_S^\alpha \alpha^2 + C_S^\beta \beta, \quad (54)$$

$$C_L(\alpha, \beta) = C_L^0 + C_L^\alpha \alpha + C_L^\beta \beta^2, \quad (55)$$

$$C_{M_1}(\alpha, \beta) = C_{M_1}^0 + C_{M_1}^\alpha \alpha + C_{M_1}^\beta \beta, \quad (56)$$

$$C_{M_2}(\alpha, \beta) = C_{M_2}^0 + C_{M_2}^\alpha \alpha + C_{M_2}^\beta \beta^2, \quad (57)$$

$$C_{M_3}(\alpha, \beta) = C_{M_3}^0 + C_{M_3}^\alpha \alpha + C_{M_3}^\beta \beta. \quad (58)$$

Here, all the constants with ‘‘C’’ in their notations are aerodynamic coefficients identified from the experimental data, as shown in Table II.

TABLE II
IDENTIFIED AERODYNAMIC COEFFICIENTS OF THE PROTOTYPE.

C_{\square}^{\square}	0	α	β
D	0.243	8.838 rad^{-2}	9.016 rad^{-2}
S	-0.082	-0.285 rad^{-2}	-2.356 rad^{-1}
L	0.159	2.938 rad^{-1}	8.103 rad^{-2}
M_1	-0.036	0.553 rad^{-1}	-0.683 rad^{-1}
M_2	0.057	0.093 rad^{-1}	5.236 rad^{-2}
M_3	0.093	-0.209 rad^{-1}	-0.356 rad^{-1}
K_1, K_2, K_3	-0.073,	-0.052,	-0.032 $\text{N} \cdot \text{m} \cdot \text{s/rad}$

Note that the aerodynamic coefficient $C_{M_3}^0 > 0$ indicates that the heading angle ψ of the prototype tends to increase during open-loop flight with $\delta_y = 0$, as shown in Fig. 14.

D. Feedback Control

In this section, we delve into the design of RGBlimp-Q, aiming to enhance its maneuverability and robustness through various experimental trials utilizing a classic PID feedback controller. Two IMUs serve as feedback sensors, positioned at both ends of the continuum body. Leveraging extended Kalman filters (EKF) and the kinematics of the continuum arm Eqs. (33)-(35), these sensors provide crucial information regarding the robot orientation and the continuum arm configuration. Figure 9 illustrates the schematic of the feedback controller.

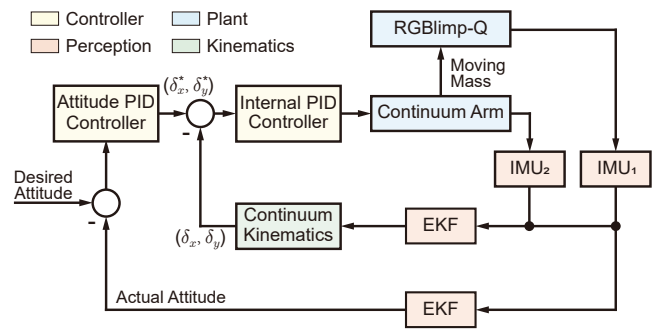


Fig. 9. Control schematic of the dual-loop PID. The internal controller regulates the continuum arm configuration in the q -parametrization, i.e., (δ_x, δ_y) . The attitude controller adjusts the orientation of RGBlimp-Q, specifically the roll, pitch, and yaw angles, utilizing both the gravitational moment of the moving mass and the aerodynamic moments.

The control objectives encompass tracking the desired configuration of the continuum arm and maintaining the desired flight orientation. To achieve this, the controller is designed into an inner loop and an outer loop, aligning with these two objectives, respectively. The inner loop controller governs the movement of the two motors controlling the continuum arm, thereby managing the tracking error in the continuum arm configuration. Additionally, the outer loop controller adjusts the robot attitude, leveraging the aerodynamic moments from the flight and the gravitational moment from the moving mass.

VI. EXPERIMENT AND DISCUSSION

In this section, we present the results of flight experiments conducted with the RGBlimp-Q prototype. Through these experiments, we evaluate the effectiveness of the design in achieving enhanced maneuverability and robustness.

A. Flight Maneuverability Experiment

The proposed design of moving mass control through the continuum arm ensures agile attitude maneuver control with reduced reliance on aerodynamics. Experimental trials are conducted to demonstrate its effectiveness.

1) *Adjusting roll and pitch angles under zero propulsion:* with the propeller shutdown and the RGBlimp-Q floating in the air, the continuum arm was controlled by the PID controller

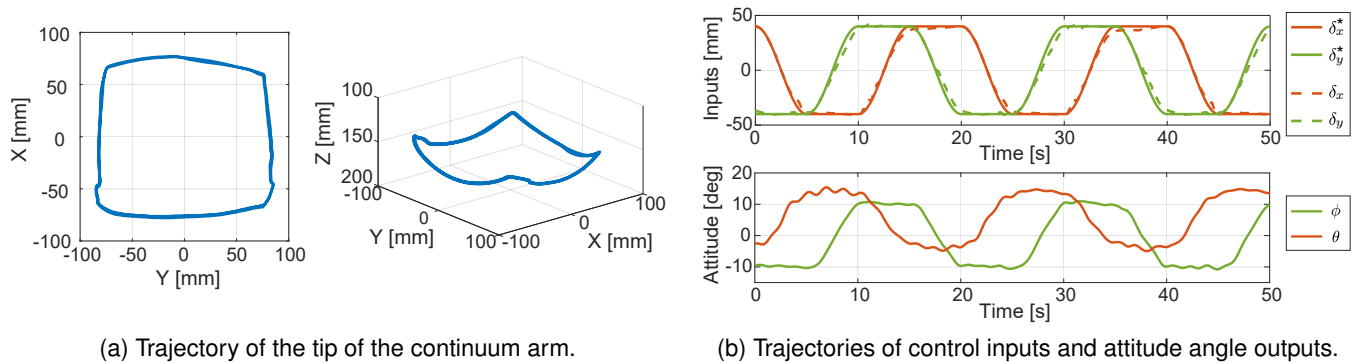


Fig. 10. Experimental results of the roll and pitch angles adjustment through the moving mass control of the continuum arm in static floating state under zero propulsion. (a) The resulting square-like trajectory of the tip of the continuum arm with its four corners tilted up. (b) The trajectories of the alternating sinusoidal control inputs δ_x and δ_y and the corresponding attitude outputs — the pitch θ and roll ϕ . The experimental results demonstrate the effectiveness of the moving mass control in attitude adjustment, even in the absence of aerodynamic moments under zero propulsion.

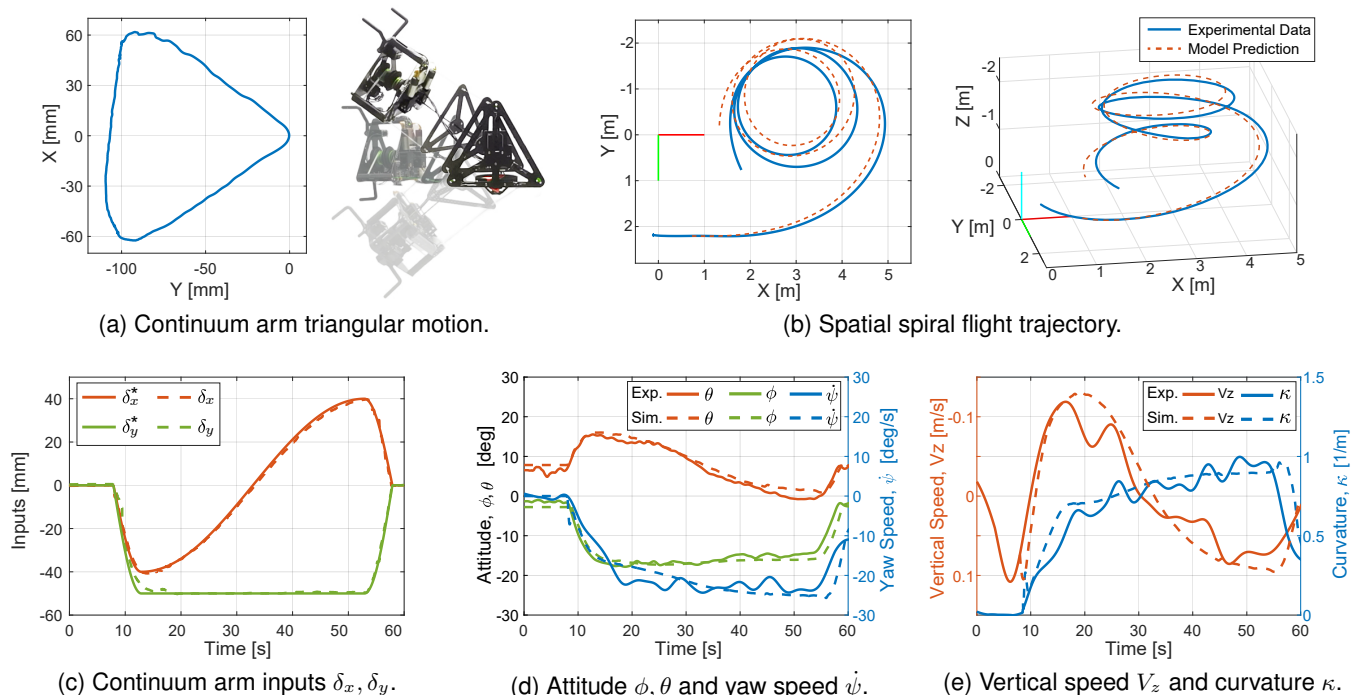


Fig. 11. Experimental results and model predictions of the dynamic flight under time-varying continuum arm inputs. The triangular motion of the tip of the continuum arm results in a spiral flight trajectory with variable curvature and vertical speed. (a) The continuum arm, following predefined control inputs, forms a triangular trajectory. (b) The flight trajectory of the robot exhibits varying curvature in the horizontal projection and varying speed in the vertical plane. (c) The continuum arm configuration (δ_x, δ_y) tracks predefined piecewise function composed of different trigonometric functions (δ_x^*, δ_y^*) . (d) The pitch θ and roll ϕ vary with the inputs δ_x and δ_y while the changing rate of yaw $\dot{\psi}$ varies with ϕ . (e) The vertical speed V_z and curvature κ are influenced by θ and ϕ through the aerodynamic yaw moment and aerodynamic lift. Note that the model prediction results in the take-off phase, spanning from 0 to 8 seconds, are not provided due to the large angle of attack, which is incompatible with the aerodynamic model used in this work.

following predefined alternating sinusoidal control inputs, i.e., δ_x^* and δ_y^* , as shown in Fig. 10b. As a result, the continuum arm alternately moves the same distance along the x_{ij} or y_{ij} directions, thus the end motion trajectory of the continuum arm formed a rectangle, as shown in Fig. 10a.

Figure 10 presents the roll and pitch angles of the RGBlimp-Q prototype adjusted by motion of the continuum arm. It is observed that the inner loop control successfully tracks the desired continuum arm configuration (δ_x^*, δ_y^*) . Further, the inputs δ_x and δ_y independently control the pitch angle and the roll angle.

2) *Maneuvering flight with moving mass control*: During flight, the RGBlimp-Q is capable of adjusting its travel direction and altitude by controlling the aerodynamic yaw moment and lift force through adjusting the roll and pitch angles, respectively. Figure 11 illustrates the experimental results of the maneuvering flight along with model predictions. The inputs, forming a triangular end motion trajectory of the continuum arm as depicted in Fig. 11a, result in a spiral flight trajectory with time-varying curvature and altitude, as shown in Fig. 11b. Similar to the previous case, the pitch and roll angles, θ and ϕ , are adjusted by the inputs δ_x and δ_y ,

respectively. Furthermore, the lift force and aerodynamic yaw moment vary according to θ and ϕ , respectively, influencing the vertical translational speed V_z and yaw rotational speed ψ .

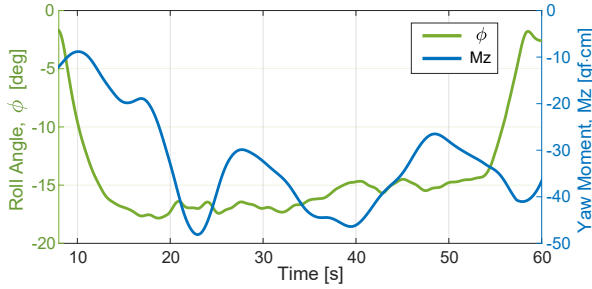


Fig. 12. The varying of roll angle ϕ leads to the according aerodynamic yaw moment M_z under a low flight speed about 0.5 m/s, resulting in the spiral flight trajectory in Fig. 11b. The yaw moment is derived from the aerodynamic model Eq.(26). Note that the model predictions in the take-off phase, spanning from 0 to 8 seconds, is not provided due to the large angle of attack, which is incompatible with the aerodynamic model used in this work.

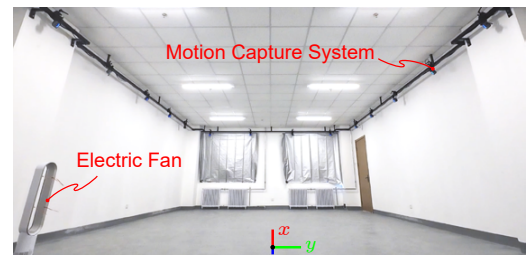
Figure 12 shows the trajectory of the aerodynamic yaw moment M_z corresponding to the roll angle ϕ in the low-speed maneuvering flight. It is observed that the negative roll angle leads to a negative aerodynamic yaw moment, resulting in an anticlockwise spiral flight observed from the top view. The RGBlimp-Q achieves an average flight speed of approximately 0.5 m/s in these series of experiments. Despite flying at low speeds, sufficient aerodynamic yaw moment and lift force are generated to facilitate maneuvering flight.

B. Flight Robustness Experiment

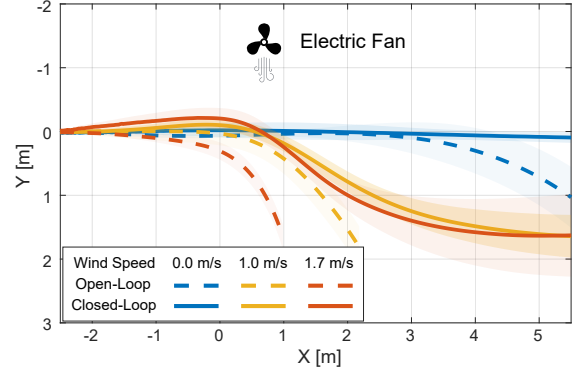
1) *Flight with a robust course direction*: extensive indoor and outdoor trials with feedback control were conducted to demonstrate the flight robustness of the RGBlimp-Q against wind disturbances. These experiments primarily focused on controlling the yaw angle to maintain a steady course direction given environmental disturbances.

For indoor flights, the experimental setup resembled that depicted in Fig. 13a. An electric fan (specifically, the *Dyson AM07 tower fan*) was adopted to create environmental wind disturbances at varying intensity levels. Three levels of wind intensity were considered, corresponding to average wind speeds of approximately 0.0, 1.0, and 1.7 m/s, respectively. Each level was tested five times, with trials consisting of both open-loop flights with predefined control and closed-loop flights with feedback control.

The comparison results of the yaw angles along with the feedback control inputs are illustrated in Fig. 14. It is worthy noting that as the wind level increases, the open-loop flight trajectory reached the boundaries of the flight area prematurely, resulting in significantly shorter flight time. It is observed that the input δ_y (green lines in the second row) effectively adjusts the roll angle ϕ (green lines in the first row), leading to further control of the flight heading angle ψ by leveraging the coupling between the aerodynamic yaw moment and the roll angle ϕ . In scenarios without environmental wind disturbance, the heading angle in open-loop flights tends to drift due to



(a) The indoor experimental setup.



(b) The comparison results of the flight trajectories.

Fig. 13. The results of the indoor flight experiment and according experimental setup. (a) Illustration of the indoor motion capture arena, equipped with an electric fan for robust flight trials. (b) The comparison results of the flight trajectories in indoor experiments between feedback control based on the continuum arm (solid lines) and open-loop flight (dash lines) under various environmental wind disturbances. The mean trajectories and corresponding standard deviations are depicted as lines and shaded areas, respectively. The location of the fan is (0.7, -1.3)m in the x - O - y plane. The comparison experimental results demonstrate the effectiveness of our continuum arm design in achieving robust flights under environmental disturbances.

inevitable asymmetries in our prototype development. The introduction of moving mass control dramatically helps mitigate this problem, ensuring flight robustness. When encountering environmental winds during flight, the moving mass control based on the continuum arm demonstrates a rapid response and effective disturbance rejection.

Figure 13 presents the indoor flight trajectories under wind disturbance observed from the top view, comparing the closed-loop and open-loop trials. The experimental results demonstrate that feedback control utilizing the continuum arm substantially enhances flight robustness in terms of maintaining the course direction.

For outdoor flights, a balloon was set up to indicate the direction and intensity of the natural wind, as shown in Fig. 15a. The wind speed varied between 0.5 m/s and 1.5 m/s with gusts up to 3 m/s, with the wind blowing from *South* to *North*. Defining the zero heading angle $\psi = 0$ point westward and considering clockwise rotations as positive, the prototype flew from *East* to *West* with a propeller thrust of $F = 8$ gf, while the feedback controller continuously adjusted the robot's heading angle to compensate for disturbances in real time.

In Fig. 15b, both the input δ_y and the roll angle ϕ exhibit similar variations, while the heading angle ψ shows an inverse trend. Specifically, when the heading angle ψ is disturbed, the moving mass control based on the proposed continuum arm

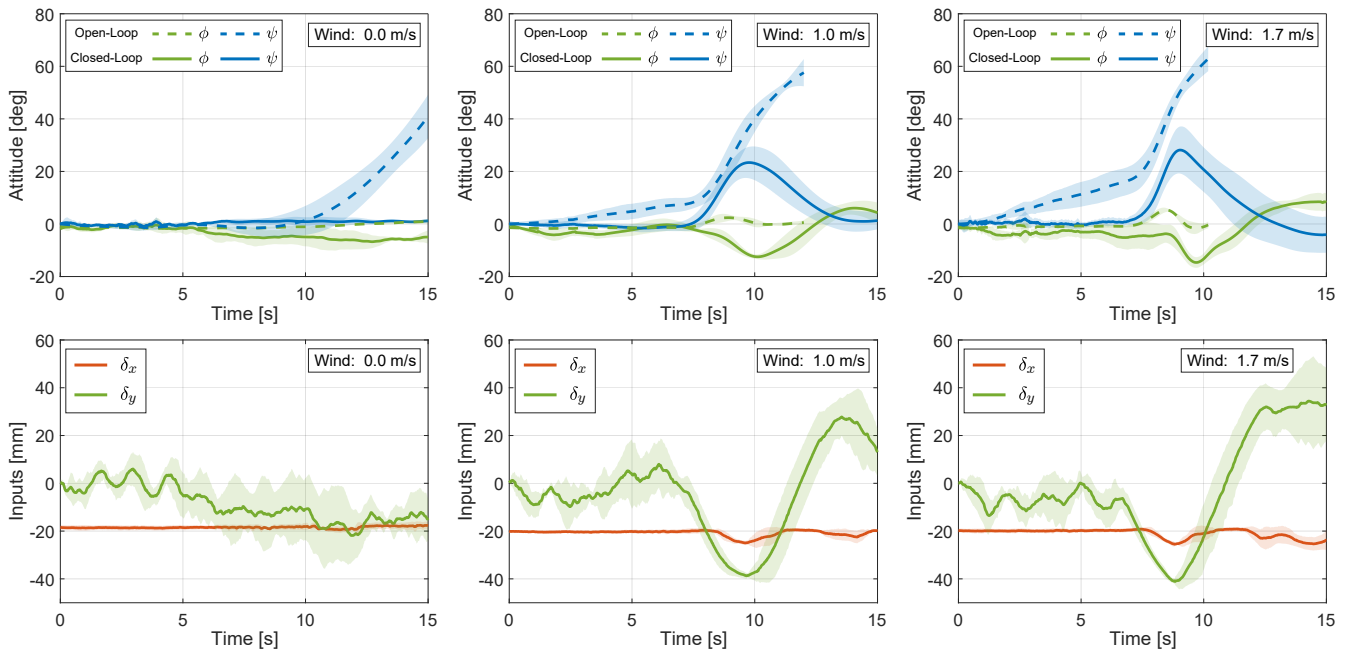
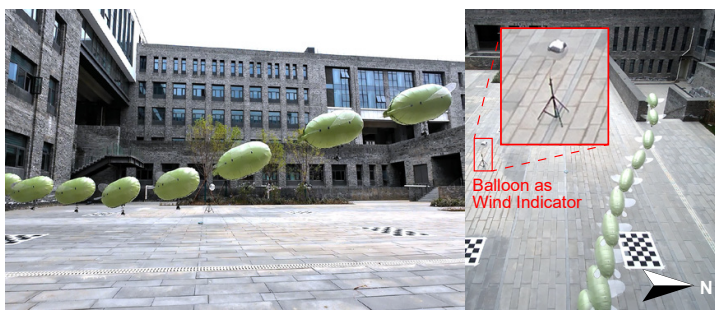
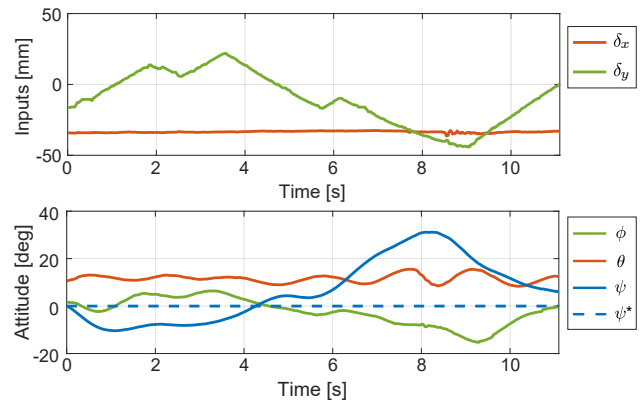


Fig. 14. The comparison results of the yaw angle (heading angle) in indoor experiments between feedback control based on the continuum arm and open-loop flight under various environmental wind disturbances. The first row presents the attitude trajectories in closed-loop (solid lines) and open-loop (dash lines) flights against three different wind levels of 0.0, 1.0, and 1.7 m/s. The pitch angles in each trial remain stable at around 13° and are omitted for brevity. The second row shows the feedback control inputs for closed-loop flights, while the inputs for open-loop flights are fixed at $\delta_x = -20$ mm and $\delta_y = 0$ mm.



(a) Flight snapshot from side and top views.



(b) Attitude angles varying with inputs and disturbance.

Fig. 15. The experimental results of the outdoor flight tests under natural wind disturbance. (a) An example outdoor test merging a series of flight snapshots from side and top views. (b) The trajectories of control inputs and resulting attitude angles with respect to flight time. The outdoor experiments demonstrate that the control input of the continuum arm δ_y restores the heading angle of the robot ψ following a gust disturbance, confirming the effectiveness of our moving mass control design.

adjusts the robot's roll angle ϕ to counteract the disturbance with the appropriate aerodynamic yaw moment. The attitude of the prototype did not fully converge to the desired zero angle by the end of the flight, with the heading reaching 6 deg. These results highlight the significant enhancement in attitude robustness achieved through the utilization of moving mass control based on the continuum arm, even in outdoor environments with complex wind disturbances.

2) *Grasping a branch for resisting excessive wind*: The effectiveness of a bio-inspired claw and associated grasping mechanism, akin to those used by birds, was demonstrated through a short flight against excessive wind (2.2 m/s) con-

ducted with teleoperation. The flight, as depicted in Fig. 16, unfolded in three distinct phases, i.e., flying straight (0 s - 3 s), encountering excessive wind (3 s - 5 s), and finally, grasping a branch to resist the wind (5 s - 7 s).

After being exposed to excessive wind, the robot quickly veered off to the side, then adjusted its attitude to navigate towards and ultimately grasp a branch for stability. In the enlarged plots of the final phase (grasping) shown in Fig. 16b, the robot experienced a slight swing due to inertia after successfully grasping the branch, before stabilizing its position in the windy environment.

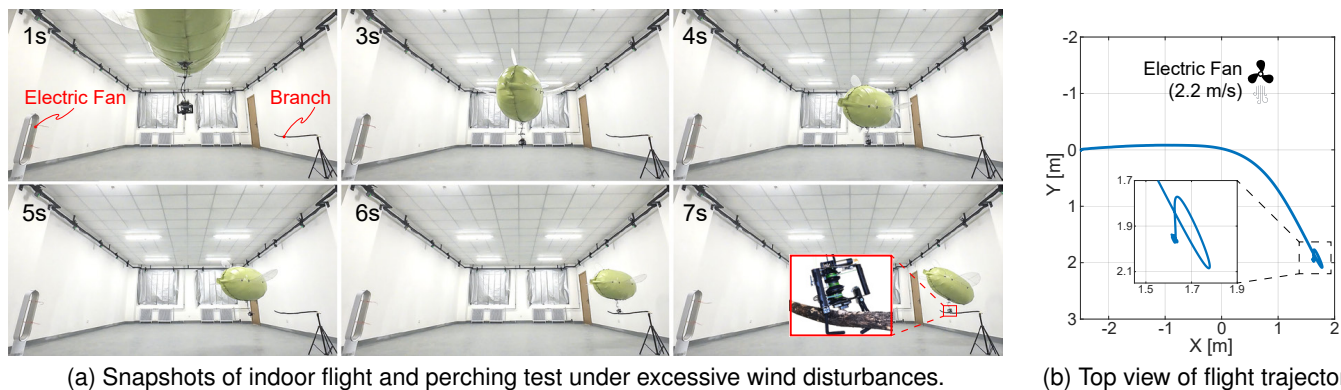


Fig. 16. Experimental results of the indoor flight and perching-on-branch test under excessive wind through the use of a bio-inspired claw for resisting wind disturbances. (a) The experimental snapshots illustrate the flight test process, starting from straight flight, encountering an excessive wind gust, and finally grasping a branch to resist the wind, mimicking bird behavior. (b) The top view of the flight trajectory recorded by the motion capture system, with a zoomed-in view of its final phase where the robot grasps the branch and maintains position in the excessive wind.

VII. CONCLUSION

In this article, we presented a comprehensive design of a bird-inspired robotic gliding blimp, termed RGBlimp-Q, engineered to exhibit enhanced maneuverability and resilience through the integration of an active continuum arm. This flying robot leverages the continuum arm for precise moving mass control, facilitating agile flight attitude maneuvers. In addition, the inclusion of a bionic claw at the end of the arm empowers the robot to grasp objects, akin to bird behavior, enabling it to withstand wind disturbances effectively. Extensive indoor and outdoor flight experiments were conducted, the results of which validated the effectiveness of the proposed design.

In future work, we will investigate more advanced control strategies such as model predict control (MPC) and learning-based control to fully exploit the capabilities of the RGBlimp-Q. Furthermore, we envision deploying the RGBlimp-Q for real-world applications such as indoor or outdoor environmental monitoring and mapping, leveraging its enhanced maneuverability and versatility to address diverse challenges. In addition, it is worthwhile to explore aerial robotic manipulators that utilize the proposed bird-inspired continuum arm, applicable to both robotic blimps and rotary-wing aerial robots.

ACKNOWLEDGMENTS

The authors would like to thank Prof. Zhongkui Li for his help in the motion capture experiment.

REFERENCES

- [1] A. Ollero, M. Tognon, A. Suarez *et al.*, "Past, present, and future of aerial robotic manipulators," *IEEE Trans. Robot.*, vol. 38, no. 1, pp. 626–645, 2021.
- [2] H. Zhong, J. Liang, Y. Chen, H. Zhang, J. Mao, and Y. Wang, "Prototype, modeling, and control of aerial robots with physical interaction: A review," *IEEE Trans. Autom. Sci. Eng.*, pp. 1–15, 2024.
- [3] F. Ruggiero, V. Lippiello, and A. Ollero, "Aerial manipulation: A literature review," *IEEE Robot. Autom. Lett.*, vol. 3, no. 3, pp. 1957–1964, 2018.
- [4] S. H. Song, G. Y. Yeon, H. W. Shon *et al.*, "Design and control of soft unmanned aerial vehicle "s-cloud"," *IEEE/ASME Trans. Mech.*, vol. 26, no. 1, pp. 267–275, 2021.
- [5] V. Mai, M. Kamel, M. Krebs *et al.*, "Local positioning system using uwb range measurements for an unmanned blimp," *IEEE Robot. Autom. Lett.*, vol. 3, no. 4, pp. 2971–2978, 2018.
- [6] C. Lu, C. Huang, J. Huang *et al.*, "A heterogeneous unmanned ground vehicle and blimp robot team for search and rescue using data-driven autonomy and communication-aware navigation," *Field Robot.*, vol. 2, pp. 557–594, 2022.
- [7] H. Cheng, Z. Sha, Y. Zhu, and F. Zhang, "RGBlimp: Robotic Gliding Blimp-design, modeling, development, and aerodynamics analysis," *IEEE Robot. Autom. Lett.*, 2023.
- [8] M. González-Álvarez, J. Dupeyroux, F. Corradi *et al.*, "Evolved neuro-morphic radar-based altitude controller for an autonomous open-source blimp," in *Proc. IEEE Int. Conf. Robot. and Autom.*, 2022, pp. 85–90.
- [9] J. Muller, A. Rottmann, L. M. Reindl *et al.*, "A probabilistic sonar sensor model for robust localization of a small-size blimp in indoor environments using a particle filter," in *Proc. IEEE Int. Conf. Robot. and Autom.*, 2009, pp. 3589–3594.
- [10] H. S. Poon, M. K. K. Lam, M. Chow *et al.*, "Noiseless and vibration-free ionic propulsion technology for indoor surveillance blimps," in *Proc. IEEE Int. Conf. Robot. and Autom.*, 2009, pp. 2891–2896.
- [11] T. Fukao, T. Oshibuchi, K. Osuka *et al.*, "Outdoor blimp robots for rescue surveillance systems," in *Proc. SICE Annual Conf.*, 2008, pp. 982–987.
- [12] S. Sharma, M. Verhoeff, F. Joosen *et al.*, "A morphing quadrotor-blimp with balloon failure resilience for mobile ecological sensing," *IEEE Robot. Autom. Lett.*, vol. 9, no. 7, pp. 6408–6415, 2024.
- [13] H. Ishida, "Blimp Robot for Three-Dimensional Gas Distribution Mapping in Indoor Environment," *AIP Conf. Proc.*, vol. 1137, no. 1, pp. 61–64, 05 2009.
- [14] C. F. Liew and T. Yairi, "Quadrotor or blimp? noise and appearance considerations in designing social aerial robot," in *Proc. ACM/IEEE Int. Conf. Hum.-Robot Interaction*, 2013, pp. 183–184.
- [15] M. Hou, Q. Tao, and F. Zhang, "Human pointing motion during interaction with an autonomous blimp," *Sci. Rep.*, vol. 12, no. 1, p. 11402, 2022.
- [16] N. Yao, E. Anaya, Q. Tao *et al.*, "Monocular vision-based human following on miniature robotic blimp," in *Proc. IEEE Int. Conf. Robot. Autom.*, 2017, pp. 3244–3249.
- [17] M. Burri, L. Gasser, M. Käch *et al.*, "Design and control of a spherical omnidirectional blimp," in *Proc. IEEE/RSJ Int. Conf. Intell. Robot. Syst.*, 2013, pp. 1873–1879.
- [18] D. St-Onge, C. Gosselin, and N. Reeves, "Dynamic modelling and control of a cubic flying blimp using external motion capture," *J. Syst. and Contr. Eng.*, vol. 229, no. 10, pp. 970–982, 2015.
- [19] Y. Wang, G. Zheng, D. Efimov *et al.*, "Disturbance compensation based control for an indoor blimp robot," in *Proc. IEEE Int. Conf. Robot. Autom.*, 2019, pp. 2040–2046.
- [20] —, "Improved altitude control method with disturbance compensation for an indoor blimp robot," in *Proc. IEEE Conf. Decision Control*, 2017, pp. 3902–3907.
- [21] Y. T. Liu, E. Price, M. J. Black *et al.*, "Deep residual reinforcement learning based autonomous blimp control," in *Proc. IEEE/RSJ Int. Conf. Intell. Robot. Syst.*, 2022, pp. 12 566–12 573.

- [22] H. Kawano, "Method for designating the wind condition in MDP-based motion planning of under-actuated blimp type uav," in *Proc. IEEE Int. Conf. Robot. Autom.*, 2007, pp. 1049–1055.
- [23] B. Wang, Z. Ma, S. Lai *et al.*, "Neural moving horizon estimation for robust flight control," *IEEE Trans. Robot.*, vol. 40, pp. 639–659, 2024.
- [24] A. Saviolo, J. Frey, A. Rathod *et al.*, "Active learning of discrete-time dynamics for uncertainty-aware model predictive control," *IEEE Trans. Robot.*, vol. 40, pp. 1273–1291, 2024.
- [25] M. O'Connell, G. Shi, X. Shi *et al.*, "Neural-fly enables rapid learning for agile flight in strong winds," *Sci. Robot.*, vol. 7, no. 66, p. eabm6597, 2022.
- [26] C. Powers, D. Mellinger, A. Kushleyev, B. Kothmann, and V. Kumar, "Influence of aerodynamics and proximity effects in quadrotor flight," in *Experimental Robotics*. Springer, 2013, pp. 289–302.
- [27] R. Lakhmani, "Kingfisher knocks bird off branch after flying into it," Accessed: Apr. 2024, [Online]. Available: <https://youtu.be/QQvOjNKXKSU>.
- [28] P. C. Khandelwal and T. L. Hedrick, "Combined effects of body posture and three-dimensional wing shape enable efficient gliding in flying lizards," *Sci. Rep.*, vol. 12, no. 1, p. 1793, 2022.
- [29] K. L. Bishop, "The relationship between 3-D kinematics and gliding performance in the southern flying squirrel, *glaucomys volans*," *J. Exp. Biol.*, vol. 209, no. 4, pp. 689–701, 2006.
- [30] C. Harvey, V. Baliga, J. Wong *et al.*, "Birds can transition between stable and unstable states via wing morphing," *Nature*, vol. 603, no. 7902, pp. 648–653, 2022.
- [31] R. Brown, "The flight of birds," *Biol. Rev.*, vol. 38, no. 4, pp. 460–489, 1963.
- [32] W. R. Roderick, M. R. Cutkosky, and D. Lentink, "Bird-inspired dynamic grasping and perching in arboreal environments," *Sci. Robot.*, vol. 6, no. 61, p. eabj7562, 2021.
- [33] "The brown-backed shrike in the wind," Accessed: Apr. 2024, [Online]. Available: <https://www.bilibili.com/video/BV1BW4y1n75r>.
- [34] Q. Tao, J. Wang, Z. Xu *et al.*, "Swing-reducing flight control system for an underactuated indoor miniature autonomous blimp," *IEEE/ASME Trans. Mech.*, vol. 26, no. 4, pp. 1895–1904, 2021.
- [35] K. Hang, X. Lyu, H. Song *et al.*, "Perching and resting—a paradigm for uav maneuvering with modularized landing gears," *Sci. Robot.*, vol. 4, no. 28, p. eaau6637, 2019.
- [36] H. Paul, K. Ono, R. Ladig *et al.*, "A multirotor platform employing a three-axis vertical articulated robotic arm for aerial manipulation tasks," in *Proc. IEEE/ASME Int. Conf. Adv. Intell. Mech.*, 2018, pp. 478–485.
- [37] J. Thomas, J. Polin, K. Sreenath *et al.*, "Avian-inspired grasping for quadrotor micro uavs," in *Proc. ASME Int. Des. Eng. Tech. Conf. and Comp. Inf. Eng. Conf.*, vol. 55935, 2013, p. V06AT07A014.
- [38] W. Stewart, E. Ajanic, M. Müller *et al.*, "How to swoop and grasp like a bird with a passive claw for a high-speed grasping," *IEEE/ASME Trans. Mech.*, vol. 27, no. 5, pp. 3527–3535, 2022.
- [39] S. Kolachalama, S. Lakshmanan *et al.*, "Continuum robots for manipulation applications: A survey," *J. Robot.*, vol. 2020, 2020.
- [40] G. Robinson and J. B. C. Davies, "Continuum robots—a state of the art," in *Proc. IEEE Int. Conf. Robot. Autom.*, vol. 4, 1999, pp. 2849–2854.
- [41] M. Coad, L. Blumenschein, S. Cutler *et al.*, "Vine robots: Design, teleoperation, and deployment for navigation and exploration," *IEEE Robot. Autom. Magaz.*, vol. PP, 10 2019.
- [42] R. K. Katzschmann, C. Della Santina, Y. Toshimitsu *et al.*, "Dynamic motion control of multi-segment soft robots using piecewise constant curvature matched with an augmented rigid body model," in *Proc. IEEE Int. Conf. Soft Robot.*, 2019, pp. 454–461.
- [43] S. Huang, D. Meng, X. Wang *et al.*, "A 3D static modeling method and experimental verification of continuum robots based on pseudo-rigid body theory," in *Proc. IEEE/RSJ Int. Conf. Intell. Robots Syst.*, 2019, pp. 4672–4677.
- [44] G. Fang, Y. Tian, Z.-X. Yang *et al.*, "Efficient jacobian-based inverse kinematics with sim-to-real transfer of soft robots by learning," *IEEE/ASME Trans. Mech.*, vol. 27, no. 6, pp. 5296–5306, 2022.
- [45] H. Cheng, H. Liu, X. Wang *et al.*, "Approximate piecewise constant curvature equivalent model and their application to continuum robot configuration estimation," in *Proc. IEEE Int. Conf. Syst. Man Cyber.*, 2020, pp. 1929–1936.
- [46] B. A. Jones and I. D. Walker, "Kinematics for multisection continuum robots," *IEEE Trans. Robot.*, vol. 22, no. 1, pp. 43–55, 2006.
- [47] C. Della Santina, A. Bicchi, and D. Rus, "On an improved state parametrization for soft robots with piecewise constant curvature and its use in model based control," *IEEE Robot. Autom. Lett.*, vol. 5, no. 2, pp. 1001–1008, 2020.
- [48] H. Cheng, H. Xu, H. Shang *et al.*, "Orientation to pose: Continuum robots shape reconstruction based on the multi-attitude solving approach," in *Proc. IEEE Int. Conf. Robot. Autom.*, 2022, pp. 3203–3209.
- [49] R. Peng, Z. Wang, and P. Lu, "Aecom: An aerial continuum manipulator with imu-based kinematic modeling and tendon-slacking prevention," *IEEE Trans. Syst. Man Cybern.*, vol. 53, no. 8, pp. 4740–4752, 2023.
- [50] R. F. Stengel, *Flight Dynamics: Second Edition*. Princeton University Press, 2022.



Hao Cheng received the Bachelor's degree in New Energy Science and Engineering (Wind Power) from North China Electric Power University, China, in 2017, and the Master's degree in Control Engineering from Tsinghua University, China, in 2021. He is currently working toward the Ph.D. degree in Mechanics at Peking University, China, under the supervision of Prof. F. Zhang. His research interests include Light-Than-Air Aerial Vehicles, Bioinspired Robotics, and Continuum Robots.



Feitian Zhang received the Bachelor's and Master's degrees in Automatic Control from Harbin Institute of Technology, Harbin, China, in 2007 and 2009, respectively, and the Ph.D. degree in Electrical and Computer Engineering from Michigan State University, East Lansing, MI, in 2014.

Feitian Zhang is currently an Associate Professor in the Department of Advanced Manufacturing and Robotics at Peking University. Prior to joining Peking University, he was an Assistant Professor in the Department of Electrical and Computer Engineering at George Mason University (GMU), Fairfax, VA, and the founding director of the Bioinspired Robotics and Intelligent Control Laboratory (BRICLab) from 2016 to 2021. His research interests include Bioinspired Robotics, Control Systems, Artificial Intelligence, Underwater Vehicles, and Aerial Vehicles.